Self-consistent, high-order spatial profiles in a model for two-fluid turbulent mixing

Brandon E. Morgan

Phys. Rev. E **104**, 015107 — Published 22 July 2021

DOI: 10.1103/PhysRevE.104.015107

Self-consistent, high-order spatial profiles in a model for two-fluid turbulent mixing

Brandon E. Morgan
Lawrence Livermore National Laboratory
Livermore, California 94550

(Dated: June 7, 2021)

A new Reynolds-averaged Navier-Stokes model is presented with the property that it admits self-consistent, high-order spatial profiles in simulations of two-fluid turbulent mixing layers. Whereas previous models have been limited by the assumption of a linear mixing profile, the present work relaxes this assumption, and as a result is shown to achieve much better agreement with experimental profiles. Similarity analysis is presented to derive constraints on model coefficients to enforce desired self-similar growth rates that are fully consistent with the high-order spatial profiles. Through this similarity analysis, it is shown that care must be taken in model construction, as it is possible to construct certain terms in such a way as to leave growth rates unconstrained. The new model, termed the k-ϕ-L-a-V model, is then applied in simulations of Rayleigh-Taylor, Richtmyer-Meshkov, and Kelvin-Helmholtz mixing layers. These simulations confirm that the expected growth parameters are recovered, and high-order spatial profiles are maintained.

I. INTRODUCTION

Significant effort has been devoted over the years to the development of Reynolds-averaged Navier-Stokes (RANS) models for variable density turbulent mixing [1–22]. A common approach in the development of many such models is to rely on self-similarity analysis to determine constraints on model coefficients that will reproduce certain expected growth parameters [5, 6, 10, 14, 15, 21, 22]. The self-similarity approach generally begins with an ansatz approximation that turbulence quantities can be written as separable functions of space and time. For instance, for an arbitrary model variable g, one might make the approximation,

$$g\left(x,t\right) = G_0\left(t\right) f\left(\chi\right) \ . \tag{1}$$

In Eq. 1, the assumed form of f determines the spatial profile of g and is only a function of the self-similar coordinate $\chi \equiv x/h$, where h is the mixing layer half-width. Starting with this separability ansatz, it then becomes possible to derive algebraic constraints on model coefficients that will enforce the ansatz. The approach is quite powerful in that its application can be used to derive constraints that will allow a model to exactly reproduce desired behavior such as the Rayleigh-Taylor (RT) growth parameter α, the Richtmyer-Meshkov (RM) growth parameter θ, and the Kelvin-Helmholtz growth parameter δ.

In previous models such as the k-L [5], k-L-a [10], and k-L-a-V [15] models, f is assumed to take a quadratic form for most turbulence variables, and profiles of the primary mixing quantity (i.e., density in RT mixing or velocity in KH mixing) are assumed to take a linear profile. These approximations simplify the analysis significantly but ultimately lead to mixing profiles that disagree with data in the tails. That is, data from high-fidelity simulation and experimental measurement generally suggests that profiles of turbulence kinetic energy (TKE) are more closely represented by a Gaussian, and mixing profiles more closely represented by an error function or a hyperbolic tangent.

Some authors have attempted to minimize this discrepancy by adjusting turbulent diffusion coefficients in an *ad hoc* fashion after first determining self-similarity constraints under the assumption of a linear mixing profile [6]. This approach can improve agreement to an extent but violates the self-similarity constraints, which can lead to unintended and hard-to-predict discrepancies in anticipated growth rates. In addition, this approach tends to have relatively little impact on the mixing profile, leading to continued discrepancy with data. More recently, Zhang *et al.* [21] have introduced an approach for setting model coefficients in the k-L model that relaxes the assumption of a quadratic profile for k to an extent. However, even this approach maintains significant restrictions on the polynomial power of the self-similar profiles for k and L, and it also relies on the ansatz of a linear mixing profile.

The present work introduces a new model, termed the k-ϕ-L-a-V model, which is developed with the explicit intent of designing a model that will admit high-order profiles for both mixing profiles and turbulence variables through self-similarity analysis. To accomplish this, the k-ϕ-L-a-V model solves a transport equation for the turbulence velocity ϕ (which can alternatively be thought of as the dissipation rate of the turbulence length scale) in addition to transport equations for turbulence kinetic energy k, turbulence length scale L, mass-flux velocity a_i, and scalar variance V. Self-similarity analysis of this model will be presented demonstrating that constraints on model coefficients can be derived that will enforce expected growth rates while maintaining the desired high-order profiles. The model is then applied in simulations of 1D RT, RM, and KH layers to verify that expected growth rates are recovered and high-order profiles are maintained.

The remainder of this work is laid out as follows. First,

in section II, the k-ϕ-L-a-V model is presented. Then, in section III, self-similarity analysis is presented to derive constraints on model coefficients necessary to reproduce expected RT, RM, and KH growth parameters. The model is then applied in simulations of 1D RT, RM, KH, and combined RT-KH mixing layers in section IV to verify that the desired behavior is in fact obtained. Results with the k-ϕ-L-a-V model are compared with results of the k-$2L$-a-V model [14–16, 22], and it is demonstrated that the high-order profiles obtained with the k-ϕ-L-a-V model are a much closer match to data. Finally, in section IV, conclusions are drawn, and recommendations are made regarding the direction of future research.

II. MODEL EQUATIONS

The k-ϕ-L-a-V model is derived from the compressible RANS equations for a two-component, non-reactive gas mixture. In the present work, an overbar denotes Reynolds averaging, and a tilde denotes mass-weighted (Favre) averaging. An arbitrary scalar, f, is decomposed as

$$f = \overline{f} + f' = \widetilde{f} + f'' \,, \tag{2}$$

where the Favre average is related to the Reynolds average through the density, ρ, according to

$$\widetilde{f} = \frac{\overline{\rho f}}{\overline{\rho}} \,. \tag{3}$$

The Reynolds stress tensor, mass-flux velocity vector, and density–specific-volume covariance are defined, respectively, in terms of the velocity vector, u_i, and the specific volume, $1/\rho$, by

$$\overline{\rho}\tau_{ij} \equiv -\overline{\rho u_i'' u_j''} \,, \tag{4a}$$

$$a_i \equiv -\overline{u_i''} \,, \tag{4b}$$

$$b \equiv -\overline{\rho' \left(\frac{1}{\rho}\right)'} \,. \tag{4c}$$

Equations (5)–(18) below summarize the k-ϕ-L-a-V model, where $\widetilde{Y}$ is the mass fraction, v is the volume fraction, μ_t is the eddy viscosity, g_j is the gravitational acceleration vector, e is the specific internal energy, ϕ is the turbulent velocity, L is the turbulent length scale, and V is the model variable for variance of the mass fraction. Subscripts H and L, as in Y_H or v_L, indicate scalar fractions associated with the heavy and light species, respectively. The model coefficients C_A, C_B, C_D, C_{p1}, C_{p2}, C_{p3}, C_{L1}, C_{L2}, C_{L3}, C_{V1}, C_{V2}, C_{V3}, N_a, N_e, N_k, N_p, N_L, N_V, N_Y, and C_{dev} are determined through similarity analysis. The model equations are

$$\frac{D\overline{\rho}}{Dt} = -\overline{\rho}\frac{\partial \widetilde{u}_i}{\partial x_i} \,, \tag{5}$$

$$\overline{\rho}\frac{D\widetilde{Y}_k}{Dt} = \frac{\partial}{\partial x_i}\left(\frac{\mu_t}{N_Y}\frac{\partial \widetilde{Y}_k}{\partial x_i}\right) \,, \tag{6}$$

$$\overline{\rho}\frac{D\widetilde{u}_j}{Dt} = \overline{\rho}g_j - \frac{\partial \overline{p}}{\partial x_j} + \frac{\partial}{\partial x_i}\left(\overline{\rho}\tau_{ij}\right) \,, \tag{7}$$

$$\begin{aligned}\overline{\rho}\frac{D\widetilde{e}}{Dt} =& -\overline{p}\frac{\partial \widetilde{u}_i}{\partial x_i} - a_i\frac{\partial \overline{p}}{\partial x_i} + C_D\frac{\overline{\rho}\phi k}{L} \\ &+ \frac{\partial}{\partial x_i}\left(\frac{\mu_t}{N_e}\frac{\partial \widetilde{e}}{\partial x_i}\right) \,,\end{aligned} \tag{8}$$

$$\begin{aligned}\overline{\rho}\frac{Dk}{Dt} =& \overline{\rho}\tau_{ij}\frac{\partial \widetilde{u}_i}{\partial x_j} + a_i\frac{\partial \overline{p}}{\partial x_i} - C_D\frac{\overline{\rho}\phi k}{L} \\ &+ \frac{\partial}{\partial x_i}\left(\frac{\mu_t}{N_k}\frac{\partial k}{\partial x_i}\right) \,,\end{aligned} \tag{9}$$

$$\begin{aligned}\overline{\rho}\frac{D\phi}{Dt} =& C_{p1}\overline{\rho}\frac{\phi^2}{L} + C_{p2}\frac{1}{\phi V^{3/8}}\overline{\rho}\tau_{ij}\frac{\partial \widetilde{u}_i}{\partial x_j} \\ &+ C_{p3}\frac{a_i}{\phi V^{3/8}}\frac{\partial \overline{p}}{\partial x_i} + \frac{\partial}{\partial x_i}\left(\frac{\mu_t}{N_p}\frac{\partial \phi}{\partial x_i}\right) \,,\end{aligned} \tag{10}$$

$$\begin{aligned}\overline{\rho}\frac{DL}{Dt} =& C_{L1}\overline{\rho}\phi + C_{L2}\overline{\rho}L\frac{\partial \widetilde{u}_i}{\partial x_i} \\ &+ C_{L3}\overline{\rho}\tau_{ij}\frac{L}{k}\frac{\partial \widetilde{u}_i}{\partial x_j} + \frac{\partial}{\partial x_i}\left(\frac{\mu_t}{N_L}\frac{\partial L}{\partial x_i}\right) \,,\end{aligned} \tag{11}$$

$$\begin{aligned}\overline{\rho}\frac{Da_j}{Dt} =& C_B\frac{b}{V^{3/8}}\frac{\partial \overline{p}}{\partial x_j} - C_A\overline{\rho}\frac{\phi}{L}a_j \\ &+ \frac{\overline{\rho}\tau_{ij}}{V^{3/8}}\left|\frac{\widetilde{v}_H}{\widetilde{Y}_H} - \frac{\widetilde{v}_L}{\widetilde{Y}_L}\right|\frac{\partial \widetilde{Y}_H}{\partial x_i} + \frac{\partial}{\partial x_i}\left(\frac{\mu_t}{N_a}\frac{\partial a_j}{\partial x_i}\right) \,,\end{aligned} \tag{12}$$

$$\begin{aligned}\overline{\rho}\frac{DV}{Dt} =& C_{V1}\mu_t\frac{\partial \widetilde{Y}_H}{\partial x_i}\frac{\partial \widetilde{Y}_H}{\partial x_i} - C_{V2}\overline{\rho}\frac{\phi}{L}V \\ &+C_{V3}V\frac{a_i}{k}\frac{\partial \overline{p}}{\partial x_i} + \frac{\partial}{\partial x_i}\left(\frac{\mu_t}{N_V}\frac{\partial V}{\partial x_i}\right) \,,\end{aligned} \tag{13}$$

where

$$\frac{D}{Dt} \equiv \frac{\partial}{\partial t} + \widetilde{u}_i\frac{\partial}{\partial x_i} \,, \tag{14}$$

$$\mu_t = \overline{\rho}L\phi \,, \tag{15}$$

$$\widetilde{S}_{ij} = \frac{1}{2}\left(\frac{\partial \widetilde{u}_i}{\partial x_j} + \frac{\partial \widetilde{u}_j}{\partial x_i}\right) - \frac{1}{3}\frac{\partial \widetilde{u}_k}{\partial x_k}\delta_{ij} \,, \tag{16}$$

$$\overline{\rho}\tau_{ij} = C_{dev} 2\mu_t \widetilde{S}_{ij} - \frac{2}{3}\overline{\rho} k \delta_{ij} \,, \tag{17}$$

and

$$b = \left(\frac{\widetilde{v}_H}{\widetilde{Y}_H} - \frac{\widetilde{v}_L}{\widetilde{Y}_L} \right)^2 V \,. \tag{18}$$

The k-ϕ-L-a-V model as it is presented above is formulated under the assumption of two-fluid mixing, as this form lends itself most easily to self-similarity analysis. As discussed in Appendix A, it is possible to formulate the model for an arbitrary number of mixing species. For simplicity, however, the remainder of the present manuscript will focus on the special formulation for two-fluid mixing.

It has long been recognized that a transport equation may be derived for any turbulence model variable of the form $\phi^m L^n$ for arbitrary exponents m and n [23–25]. Moreover, transport equations of this form are generally expected to include right-hand-side contributions due to shear production, buoyancy production, dissipation, and diffusive transport [25]. Although the transport equation for ϕ given by Eq. 10 is arrived at fairly heuristically, we note that it is dimensionally correct, Galilean invariant, and includes terms corresponding to the four contributions previously mentioned. Although models involving a transport equation for turbulence velocity (i.e., $m = 1$, $n = 0$) are not frequently encountered, there have been some explorations of this form [26].

Generally speaking, what sets the present work apart from previous models that have explored use of the turbulence velocity as a primary turbulence variable is the presence of a second turbulence velocity in the present model in the form of $\sqrt{k}$. As similarity analysis will reveal in section III, the ratio $\frac{\phi}{\sqrt{k}}$ is expected to approach a constant value at the center of a mixing layer in both buoyancy-driven and shear-driven mixing regimes. However, the constant that is approached is different for the two regimes, similar to the behavior of the ratio of transport to destruction length scales in two-length-scale models [14]. Thus, the utility of having two turbulence velocities is in providing the necessary degree of freedom to simultaneously match growth rates in both the buoyancy-driven and shear-driven regimes. While it may be possible to develop a two-length-scale model conforming to the same high-order spatial profiles as the present two-velocity model, the analysis was found to simplify considerably using the two-velocity form of the present work.

A peculiar feature of the k-ϕ-L-a-V model worth noting at this time is the appearance of the scalar variance V in the denominator of production terms in Eqs. 10 and 12. The necessity for this development will be discussed in greater detail in section III, but the presence of V in shear production terms indicates that the present model *requires* scalar transport. In other words, the k-ϕ-L-a-V model would not correctly predict free shear growth in a single fluid flow unless one fluid stream has been injected with a passive scalar. In this sense, the k-ϕ-L-a-V should be thought of as a model specifically for two-fluid mixing. With this caveat noted, the next section discusses development of the model under the assumption of high-order spatial profiles.

III. SIMILARITY ANALYSIS

Self-similarity analysis is a powerful tool that has been applied previously to derive constraints on model coefficients in the k-L [5, 12], k-L-a [10], k-2L-a [14], and k-2L-a-V [15, 22] models. In the present work, we relax the assumption of a linear mass fraction profile that was utilized in all of these previous works. To begin, a change of variable is introduced in terms of the mixing layer half-width $h(t)$ such that $\chi \equiv x/h$. In the following sections, it is assumed that a scalar profile across the mixing layer is given by

$$Y(\chi) = \frac{1}{A} \int_{-1}^{\chi} \left(1 - \hat{\chi}^2\right)^{n_Y} \mathrm{d}\hat{\chi} \,. \tag{19}$$

In Eq. 19, n_Y is an arbitrary exponent, and A is a normalization constant given in terms of the gamma function Γ by

$$A = \sqrt{\pi} \frac{\Gamma(n_Y + 1)}{\Gamma\left(n_Y + \frac{3}{2}\right)} \,. \tag{20}$$

In the case of an RT or RM mixing layer, the scalar profile represents species mass fraction across the mixing layer, while in the case of a KH mixing layer the scalar profile is a passive tracer in one fluid stream.

In all cases, the self-similarity ansatz is applied such that we assume turbulence variables are separable functions of time and space. From prior work [10], it has been shown that L must assume a spatial profile of the form $f^{1/2}$, where $f = 1 - \chi^2$, in order to constrain the relationship between L and h. Additionally, it is recognized that in order to maintain consistency with the diffusive terms, the eddy viscosity must assume a spatial profile of the form f^1, which constrains the spatial profile of ϕ to also follow a profile of the form $f^{1/2}$. With these constraints in place, the separability ansatz is summarized according to,

$$k(\chi, t) = K_0(t) f^{n_k}(\chi) \,, \tag{21a}$$
$$\phi(\chi, t) = P_0(t) f^{1/2}(\chi) \,, \tag{21b}$$
$$L(\chi, t) = L_0(t) f^{1/2}(\chi) \,, \tag{21c}$$
$$a(\chi, t) = A_0(t) f^{n_k}(\chi) \,, \tag{21d}$$
$$V(\chi, t) = V_0(t) f^{2n_Y + 1}(\chi) \,. \tag{21e}$$

Generally speaking, there is no reason why the subsequent analysis could not be performed for arbitrary exponents n_Y and n_k; however, *a priori* observation suggests that optimal agreement with experimental data occurs when $n_k = n_Y + 1$. Moreover, it is found that best agreement occurs when $n_Y \approx 3/2$. Thus, to simplify the algebra required, moving forward it is assumed $n_Y = 3/2$ and $n_k = 5/2$.

As a final comment before continuing on to the details of self-similarity analysis, it is interesting to note that the k-ϕ-L-a-V model does not utilize separate transport equations for production and destruction length scales like the k-2L-a or k-2L-a-V models [14, 22]. By instead utilizing the ϕ equation, the k-ϕ-L-a-V model effectively transports two different turbulent velocities: (1) ϕ which is utilized in both destruction and diffusive transport terms and (2) $\sqrt{k}$ which couples back to the momentum equation through the isotropic Reynolds stresses. As the following analysis will show, this approach is able to recover the same self-similar growth parameters for RT and KH flow as the two-length-scale models.

A. Similarity of an RT mixing layer

1. Similarity of the L equation

For a 1D RT mixing layer in the limit of zero Atwood number, Eq. 11 reduces to

$$\rho\frac{DL}{Dt} = C_{L1}\overline{\rho}\phi + \frac{\partial}{\partial x}\left(\frac{\mu_t}{N_L}\frac{\partial L}{\partial x}\right) . \tag{22}$$

Assuming $L_0 = \beta h$ for some proportionality constant β and substituting Eqs. 21 into Eq. 22 then results in the following expression after some algebra

$$\dot{L}_0 = P_0\left[2\frac{\beta^2}{N_L} - C_{L1}\right]\chi^2 + P_0\left[C_{L1} - \frac{\beta^2}{N_L}\right] , \tag{23}$$

where the dot notation has been used to indicate differentiation with respect to time. The separability ansatz requires the term that is quadratic in χ must vanish, which is satisfied if $\beta^2 = C_{L1}N_L/2$. Utilizing this constraint further reduces Eq. 23 to

$$\dot{L}_0 = \frac{C_{L1}}{2}P_0 . \tag{24}$$

2. Similarity of the a equation

Similarly, for a 1D RT mixing layer, Eq. 12 reduces to

$$\begin{aligned}\overline{\rho}\frac{Da}{Dt} =& C_B\frac{b}{V^{3/8}}\frac{\partial\overline{p}}{\partial x} - C_A\overline{\rho}a\frac{\phi}{L} \\ &- \frac{2}{3}\frac{\overline{\rho}k}{V^{3/8}}\left|\frac{\widetilde{v}_H}{\widetilde{Y}_H} - \frac{\widetilde{v}_L}{\widetilde{Y}_L}\right|\frac{\partial\widetilde{Y}_H}{\partial x} + \frac{\partial}{\partial x}\left(\frac{\mu_t}{N_a}\frac{\partial a}{\partial x}\right) .\end{aligned} \tag{25}$$

Note at this point the presence of $V^{3/8}$ in the denominator of the production terms in Eq. 25. Since V is unitless and approaches a predictable steady-state value, it is used here effectively as a correction to the expected spatial profiles for the two production terms such that each term on the right-hand-side of Eq. 25 should conform to the expected f^{n_k} profile. Recognize that this is only necessary because of the high-order nature of the mixing profile. If low-order profiles are assumed, as in previous models, no such correction is necessary.

By applying the low-Atwood number approximation that $\overline{\rho} \approx (\rho_H + \rho_L)/2$, it can be shown

$$\left(\frac{\widetilde{v}_H}{\widetilde{Y}_H} - \frac{\widetilde{v}_L}{\widetilde{Y}_L}\right)^2 = \left(\frac{2A_T}{1 - A_T^2}\right)^2 , \tag{26}$$

where $A_T \equiv (\rho_H - \rho_L)/(\rho_H + \rho_L)$ is the conventional Atwood number. Utilizing Eq. 24 to expand the material derivative, recognizing for a hydrostatic mixing layer that $\frac{\partial\overline{p}}{\partial x} = -\overline{\rho}g$, and substituting Eqs. 21 and 26 into Eq. 25 leads to an expression similar in form to Eq. 23. The resulting expression contains second-moment terms proportional to χ^2 which must simultaneously go to zero with zero-moment terms. Satisfaction of this requirement introduces the constraint that $N_a = 5N_L$, which reduces both second-moment and zero-moment terms to the same expression,

$$\begin{aligned}\dot{A}_0 =& -\left(C_A + \frac{4A_T\beta}{3AV_0^{3/8}}\frac{K_0}{A_0P_0} + \frac{C_{L1}}{2}\right)\frac{A_0P_0}{L_0} \\ &- 4C_BV_0^{5/8}A_T^2g .\end{aligned} \tag{27}$$

3. Similarity of the ϕ equation

For the 1D RT mixing layer under consideration, Eq. 10 reduces to

$$\overline{\rho}\frac{D\phi}{Dt} = C_{p1}\overline{\rho}\frac{\phi^2}{L} - C_{p3}\overline{\rho}\frac{a}{\phi V^{3/8}}g + \frac{\partial}{\partial x}\left(\frac{\mu_t}{N_p}\frac{\partial\phi}{\partial x}\right) . \tag{28}$$

Following the same approach as before, Eqs. 21 and 24 are substituted into Eq. 28, and the resulting expression requires $N_p = N_L$. Substitution of this constraint back then reduces the ϕ equation to

$$\dot{P}_0 = \left(C_{p1} - \frac{C_{L1}}{2}\right)\frac{P_0^2}{L_0} - C_{p3}\frac{A_0}{P_0V_0^{3/8}}g . \tag{29}$$

In addition, it is anticipated that A_0 and P_0 should be related according to $A_0 = C_a P_0$, for some proportionality constant C_a. One way to reduce Eqs. 27 and 29 to the same expression is if the following constraints are satisfied

$$C_a = -2A_T\sqrt{C_B}\,, \tag{30}$$

$$C_{p3} = V_0\,, \tag{31}$$

and

$$C_A = \frac{2\beta}{3AV_0^{3/8}\sqrt{C_B}}\frac{K_0}{P_0^2} - C_{p1}\,. \tag{32}$$

If we now invoke the ansatz that $h = \alpha A_T g t^2$, we can utilize Eq. 24 and substitute into Eq. 29 to arrive at an expression for the RT growth parameter α

$$\alpha = \frac{C_{L1}V_0^{5/8}\sqrt{C_B}}{2\beta\left(3 - 4\frac{C_{p1}}{C_{L1}}\right)}\,. \tag{33}$$

At this point, it is somewhat easier to highlight the utility of having $V^{3/8}$ in the denominator of the buoyancy production term in the ϕ equation. In order to derive similarity constraints, each term in Eq. 28 must conform to the same spatial profile. As discussed previously, β can only be fixed as a constant when L takes an $f^{1/2}$ profile. This requirement fixes the profile for ϕ to be $f^{1/2}$ as well. Since a must have the same spatial profile as k, which we want to have a higher-order profile of the form f^{n_k}, the buoyancy production term in the ϕ equation must assume a form $\overline{\rho}aF^{-1}g$, where F has units of velocity and a spatial profile $f^{n_k-1/2}$. A second consideration for the form of F is that one must be able to derive a constraint on α, which arises from the reduced ϕ equation as in Eqs. 29 and 33. It turns out that if the construction of $F = k/\phi$ is used, α assumes a dependence on the ratio P_0^2/K_0, which cannot be uniquely constrained through similarity analysis. Similarly, if $F = k/\phi$, the RT growth rate also cannot be constrained. Thus, it is desirable to construct F in such a way as to avoid this outcome, which is what motivates the current form. As the next subsection will discuss, V_0 can be shown to reach a predictable steady-state value, which enables α to be constrained according to Eq. 33.

4. *Similarity of the V equation*

For a 1D incompressible mixing layer, the RT mixedness parameter is defined by

$$\Theta_{RT} \equiv \frac{\int_{-1}^{1}\overline{Y_H Y_L}\mathrm{d}\chi}{\int_{-1}^{1}\overline{Y}_H\overline{Y}_L\mathrm{d}\chi} = 1 - \frac{\int_{-1}^{1}V\mathrm{d}\chi}{\int_{-1}^{1}\overline{Y}_H\overline{Y}_L\mathrm{d}\chi}\,. \tag{34}$$

To simplify Eq. 34, recognize for $n_Y = 3/2$,

$$V_0\int_{-1}^{1}\left(1-\chi^2\right)^{2n_Y+1}\mathrm{d}\chi = V_0\frac{256}{315}\,, \tag{35}$$

and

$$\begin{aligned}\int_{-1}^{1}\overline{Y}_H\overline{Y}_L\mathrm{d}\chi = &\int_{-1}^{1}\left[\frac{1}{A}\int_{-1}^{\chi}\left(1-\hat{\chi}^2\right)^{n_Y}\mathrm{d}\hat{\chi}\right]\times \\ &\left[1-\frac{1}{A}\int_{-1}^{\chi}\left(1-\hat{\chi}^2\right)^{n_Y}\mathrm{d}\hat{\chi}\right]\mathrm{d}\chi \\ \approx\ & 0.234\,.\end{aligned} \tag{36}$$

Substituting Eqs. 35 and 36 back into Eq. 34 and rearranging to solve for V_0 gives

$$V_0 \approx 0.288\left(1-\Theta_{RT}\right)\,. \tag{37}$$

The V equation for a 1D RT mixing layer is then given by

$$\begin{aligned}\overline{\rho}\frac{DV}{Dt} =& C_{V1}\mu_t\frac{\partial\widetilde{Y}_H}{\partial x}\frac{\partial\widetilde{Y}_H}{\partial x} - C_{V2}\overline{\rho}\frac{\phi}{L}V \\ &+C_{V3}V\frac{a}{k}\overline{\rho}g + \frac{\partial}{\partial x}\left(\frac{\mu_t}{N_V}\frac{\partial V}{\partial x}\right)\,.\end{aligned} \tag{38}$$

Recognizing from Eq. 37 that $\dot{V}_0 = 0$ and substituting Eqs. 21 and 26 into Eq. 38, one arrives at an expression that requires $N_V = 8N_L$. When this constraint is applied, the following expression is obtained

$$\begin{aligned}0 = &\frac{C_{V1}C_{L1}N_L}{2A^2} - \left(C_{V2}+\frac{C_{L1}}{2}\right)V_0 \\ &+2C_{V3}\sqrt{C_B}V_0\frac{K_0}{L_0}A_T g\,.\end{aligned} \tag{39}$$

Equation 39 can then be rearranged to solve for a constraint on C_{V3},

$$C_{V3} = \frac{1}{2\sqrt{C_B}V_0A_Tg}\frac{L_0}{K_0}\left[\left(C_{V2}+\frac{C_{L1}}{2}\right)V_0 - \frac{C_{V1}C_{L1}N_L}{2A^2}\right]\,, \tag{40}$$

where V_0 has been determined previously in Eq. 37.

5. *Similarity of the k equation*

For the hydrostatic 1D RT mixing layer, Eq. 9 becomes

$$\overline{\rho}\frac{Dk}{Dt} = -\overline{\rho}ag - C_D\frac{\overline{\rho}\phi k}{L} + \frac{\partial}{\partial x}\left(\frac{\mu_t}{N_k}\frac{\partial k}{\partial x}\right)\,. \tag{41}$$

As before, substituting into Eq. 41 results in an expression that requires $N_k = 5N_L$ to simultaneously satisfy the second-moment and zero-moment terms. Imposing this constraint then reduces the k equation to

$$\dot{K}_0 = 2\sqrt{C_B}P_0 A_T g - \left(C_D + \frac{C_{L1}}{2}\right)\frac{P_0 K_0}{L_0}\,. \tag{42}$$

Continuing, it is assumed that K_0 should be proportional to the mixing layer growth rate according to $\sqrt{K_0} = \gamma\dot{h} = 2\gamma\alpha A_T g t$ for some proportionality constant γ. Substituting this expression back into Eq. 42, the following expression for γ can be obtained

$$\gamma^2\alpha = \frac{\beta\sqrt{C_B}}{2C_{L1}\left(\frac{C_D}{C_{L1}}+1\right)}\,. \tag{43}$$

This allows one to write

$$\frac{K_0}{L_0} = \frac{4\gamma^2\alpha}{\beta}A_T g = \frac{2\sqrt{C_B}}{C_{L1}\left(\frac{C_D}{C_{L1}}+1\right)}A_T g\,. \tag{44}$$

In addition,

$$\frac{\sqrt{K_0}}{P_0} = \frac{2\gamma\alpha A_T g t}{\frac{4}{C_{L1}}\beta\alpha A_T g t} = \frac{C_{L1}}{2}\frac{\gamma}{\beta}\,, \tag{45}$$

or, after substituting Eqs. 43 and 33,

$$\frac{K_0}{P_0^2} = \frac{1}{4V_0^{5/8}}\frac{3-4\frac{C_{p1}}{C_{L1}}}{\frac{C_D}{C_{L1}}+1}\,. \tag{46}$$

Then, substituting Eq. 46 back into Eq. 32 results in the following complete constraint for C_A

$$C_A = \frac{\beta}{6AV_0\sqrt{C_B}}\frac{3-4\frac{C_{p1}}{C_{L1}}}{\frac{C_D}{C_{L1}}+1} - C_{p1}\,. \tag{47}$$

Similarly, substituting Eq. 44 back into Eq. 40 results in a complete constraint for C_{V3}.

$$C_{V3} = \frac{1}{V_0 C_{L1}\left(\frac{C_D}{C_{L1}+1}\right)}\times \left[\left(C_{V2}+\frac{C_{L1}}{2}\right)V_0 - \frac{C_{V1}C_{L1}N_L}{2A^2}\right]\,. \tag{48}$$

6. *Energy balance in an RT mixing layer*

The energy balance within a 1D RT mixing layer can be written as

$$E_K(t) = \Delta\mathrm{PE} - \Psi\,. \tag{49}$$

where E_K is the total turbulence kinetic energy integrated across the layer, ΔPE is the change in potential energy over time, and Ψ is the energy dissipated into internal energy given by

$$\Psi(t) = \int_0^t\int_{-h}^{h} C_D\overline{\rho}\frac{\phi k}{L}\mathrm{d}x\mathrm{d}t\,. \tag{50}$$

By substituting Eqs. 50, 19, and 21, into Eq. 49 and then differentiating with respect to time, the following additional constraint derived

$$C_B = \frac{1}{8n_k^2A^2}\frac{C_{L1}}{N_L} = \frac{1}{50A^2}\frac{C_{L1}}{N_L}\,. \tag{51}$$

7. *Similarity of the scalar and internal energy equations*

The procedure for performing similarity analysis of the scalar and internal energy equations follows closely the approach outlined in previous subsections. Eqs. 21 and 24 are substituted into Eqs. 6 and 8, and constraints are sought that simultaneously satisfy the second-moment expressions and the zero-moment expressions. For the sake of brevity, the details of these analyses are omitted here, but the result is the derivation of the following additional constraints on diffusion coefficients N_e and N_Y

$$N_e = N_Y = N_k\,. \tag{52}$$

B. Similarity of a KH mixing layer

The case of a quasi-1D shear layer is now considered such that u_x is a linear function of a single spatial dimension, y, and $u_y = 0$. In terms of the similarity variable, $\chi = y/h(t)$,

$$\widetilde{u}_x(\chi) = \begin{cases} U_2, & \chi \geq 1 \\ U_c\left[1 - \mathcal{A} + 2\mathcal{A}Y_u(\chi)\right], & -1 < \chi < 1 \\ U_1, & \chi \leq -1 \end{cases} \tag{53}$$

where Y_u is an indicator function that takes a similar form to Eq. 19,

$$Y_u(\chi) = \frac{1}{A_u}\int_{-1}^{\chi}\left(1-\hat{\chi}^2\right)^{n_u}\mathrm{d}\hat{\chi} \tag{54}$$

In Eq. 54, *a priori* observation suggests that $n_u = 3/4$ should provide good agreement with experimental velocity profiles. Thus, for $n_u = 3/4$,

$$A_u = \sqrt{\pi}\frac{\Gamma\left(\frac{3}{4}+1\right)}{\Gamma\left(\frac{3}{4}+\frac{3}{2}\right)} \approx 1.4378\,. \tag{55}$$

The convective velocity is then defined as

$$U_c = \frac{U_2 + U_1}{2}\,, \tag{56}$$

and $\mathcal{A}$ is the KH-analogue Atwood number defined by

$$\mathcal{A} = \frac{U_2 - U_1}{U_2 + U_1}\,. \tag{57}$$

1. Similarity of the L equation

For the quasi-1D KH mixing layer, Eq. 11 reduces to

$$\begin{aligned}\overline{\rho}\frac{DL}{Dt} =& C_{L1}\overline{\rho}\phi + C_{L3}\frac{L}{k}\left[C_{dev}\overline{\rho}L\phi\left(\frac{\partial\widetilde{u}_x}{\partial y}\right)^2\right] \\ &+ \frac{\partial}{\partial y}\left(\frac{\mu_t}{N_L}\frac{\partial L}{\partial y}\right)\,,\end{aligned} \tag{58}$$

Following a similar approach as before, it is assumed that L_0 is proportional to h such that $L_0 = \beta h$. Substituting Eqs. 21 and 53 into Eq. 58 results in second-moment and zero-moment expressions that are reduced only if

$$\beta^2 = \frac{C_{L1}N_L A_u^2}{2A_u^2 - \Phi N_L C_{L3} C_{dev}}\,, \tag{59}$$

where Φ is the inverse of the KH turbulence intensity defined according to

$$\Phi \equiv \frac{\Delta U^2}{K_0}\,. \tag{60}$$

Utilizing Eq. 59 reduces the L equation to

$$\dot{L}_0 = \frac{C_{L1}A_u^2}{2A_u^2 - \Phi N_L C_{L3} C_{dev}} P_0\,. \tag{61}$$

2. Similarity of the momentum equation

For an incompressible shear layer described by Eq. (53) with no body force, Eq. 7 reduces to:

$$\overline{\rho}\frac{D\widetilde{u}_x}{Dt} = \frac{\partial}{\partial y}\left(\overline{\rho}\tau_{xy}\right)\,. \tag{62}$$

Substituting into Eq. (62) gives

$$\frac{D\widetilde{u}_x}{Dt} = C_{dev}L_0P_0\left(\frac{\partial f}{\partial y}\frac{\partial\widetilde{u}_x}{\partial y} + f\frac{\partial^2\widetilde{u}_x}{\partial y^2}\right)\,. \tag{63}$$

Evaluating the derivatives and substituting Eqs. 59 and 61 into Eq. 63 yields the following constraint

$$\frac{2}{7N_L} = C_{dev}\,. \tag{64}$$

3. Similarity of the V equation

For the KH mixing layer under consideration, it is assumed that one of the fluid streams is injected with a passive tracer Y. As before, it is assumed that this tracer has a profile given by

$$Y(\chi) = \frac{1}{A_Y}\int_{-1}^{\chi}\left(1-\hat{\chi}^2\right)^{3/2}\mathrm{d}\hat{\chi}\,, \tag{65}$$

where

$$A_Y = \sqrt{\pi}\frac{\Gamma\left(\frac{5}{2}\right)}{\Gamma(3)} = \frac{3\pi}{8}\,. \tag{66}$$

The model equation for the variance of Y in the pseudo-1D KH mixing layer is then given by

$$\overline{\rho}\frac{DV}{Dt} = C_{V1}\mu_t\frac{\partial\widetilde{Y}}{\partial y}\frac{\partial\widetilde{Y}}{\partial y} - C_{V2}\overline{\rho}\frac{\phi}{L}V + \frac{\partial}{\partial y}\left(\frac{\mu_t}{N_V}\frac{\partial V}{\partial y}\right)\,. \tag{67}$$

Following the familiar procedure, Eq. 67 is reduced when $N_Y = 8N_L$, which results in the following expression

$$C_{V1}\frac{\beta^2}{A_Y^2} - C_{V2}V_0 - \frac{\beta^2}{N_L}V_0 = 0\,. \tag{68}$$

Similar to the approach described in Eqs. 34 through 36, it is recognized that V_0 should reach a constant value $V_0 \approx 0.288\left(1-\Theta_{KH}\right)$ in terms of the KH mixedness, Θ_{KH}. Then, rearranging Eq. 68 to solve for C_{V1} gives

$$\begin{aligned}C_{V1} = &\,0.288\left(1-\Theta_{KH}\right)\times \\ &\left[\frac{2C_{V2}A_Y^2A_u^2 - C_{V2}A_Y^2\Phi N_L C_{L3}C_{dev} + C_{L1}A_Y^2A_u^2}{N_L C_{L1}A_u^2}\right]\,.\end{aligned} \tag{69}$$

4. Similarity of the k equation

Equation 9 reduces to the following for the KH mixing layer under consideration

$$\overline{\rho}\frac{Dk}{Dt} = \overline{\rho}\tau_{xy}\frac{\partial \widetilde{u}_x}{\partial y} - C_D\frac{\overline{\rho}\phi k}{L} + \frac{\partial}{\partial x_i}\left(\frac{\mu_t}{N_k}\frac{\partial k}{\partial y}\right) . \quad (70)$$

Recognizing for a steady-state shear layer that $\dot{K}_0 = 0$ and simplifying as before, Eq. 70 is reduced when $N_k = 5N_L$, which reduces it to

$$C_{dev}\frac{\beta^2\Delta U^2}{A_u^2}\frac{P_0}{L_0} - \frac{5\beta^2}{N_k}\frac{K_0P_0}{L_0} - C_D\frac{K_0P_0}{L_0} = 0 . \quad (71)$$

Substituting Eq. 59 into Eq. 70, the following expression can then be obtained for the KH turbulence intensity

$$\Phi^{-1} = \frac{N_L C_{dev}\left(1 + C_{L3}\frac{C_D}{C_{L1}}\right)}{A_u^2\left(1 + 2\frac{C_D}{C_{L1}}\right)} . \quad (72)$$

Or alternatively, by rearranging Eq. 72, the following constraint can be determined for C_{L3}

$$C_{L3} = \frac{C_{L1}}{C_D}\left(\frac{A_u^2\left(1 + 2\frac{C_D}{C_{L1}}\right)\Phi^{-1}}{N_L C_{dev}} - 1\right) . \quad (73)$$

5. Similarity of the ϕ equation

The ϕ equation for the quasi-1D KH mixing layer is given by

$$\overline{\rho}\frac{D\phi}{Dt} = C_{p1}\overline{\rho}\frac{\phi^2}{L} + C_{p2}\frac{1}{\phi V^{3/8}}\overline{\rho}\tau_{xy}\frac{\partial \widetilde{u}_x}{\partial y} + \frac{\partial}{\partial y}\left(\frac{\mu_t}{N_p}\frac{\partial \phi}{\partial y}\right) . \quad (74)$$

Similar to the approach for the k equation, it is recognized also that $\dot{P}_0 = 0$ for a steady-state KH mixing layer. Then, substituting into and simplifying Eq. 74 requires $N_p = N_L$, which results in the following

$$C_{p1}\frac{P_0^2}{L_0} + \frac{1}{A_u^2}\frac{1}{L_0V_0^{3/8}}C_{p2}C_{dev}\Delta U^2\beta^2 - \frac{\beta^2}{N_p}\frac{P_0^2}{L_0} = 0 . \quad (75)$$

Substituting Eq. 59 into Eq. 75 and rearranging leads to the following expression

$$\frac{P_0^2}{\Delta U^2} = \frac{C_{p2}N_L C_{dev}}{A_u^2V_0^{3/8} - V_0^{3/8}\frac{C_{p1}}{C_{L1}}\left(2A_u^2 - \Phi N_L C_{L3}C_{dev}\right)} . \quad (76)$$

6. Mixing layer growth parameter

For the case of a spatially evolving shear layer the non-dimensional growth rate δ is defined as:

$$\delta \equiv \frac{dh}{dx} . \quad (77)$$

It is therefore possible to write for a temporally evolving shear layer:

$$\dot{h} = \frac{dh}{dx}\frac{dx}{dt} = \delta U_c . \quad (78)$$

Recalling that $L_0 = \beta h$ and substituting Eqs. 59 and 76 into Eq. 78, the following additional constraint is determined

$$C_{p2} = \left(\frac{\delta}{\mathcal{A}}\right)^2\frac{\left[2A_u^2 - \Phi N_L C_{L3}C_{dev}\right]}{4A_u^2C_{L1}C_{dev}}\times \left[A_u^2V_0^{3/8} - V_0^{3/8}\frac{C_{p1}}{C_{L1}}\left(2A_u^2 - \Phi N_L C_{L3}C_{dev}\right)\right] . \quad (79)$$

C. Decaying homogeneous isotropic turbulence

In the absence of mean velocity or pressure gradients, the model equations reduce to

$$\frac{\mathrm{d}k}{\mathrm{d}t} = -C_D\frac{\phi k}{L} , \quad (80)$$

$$\frac{\mathrm{d}L}{\mathrm{d}t} = C_{L1}\phi , \quad (81)$$

$$\frac{\mathrm{d}\phi}{\mathrm{d}t} = C_{p1}\frac{\phi^2}{L} , \quad (82)$$

$$\frac{\mathrm{d}V}{\mathrm{d}t} = -C_{V2}\frac{\phi V}{L} . \quad (83)$$

These equations are solved in terms of a reference time, t_0 and decay exponents, n and m:

$$k = K_0\left(1 + \frac{t}{t_0}\right)^{-n} , \quad (84a)$$

$$L = L_0\left(1 + \frac{t}{t_0}\right)^{1-n/2} , \quad (84b)$$

$$\phi = P_0\left(1 + \frac{t}{t_0}\right)^{-n/2} , \quad (84c)$$

$$V = V_0\left(1 + \frac{t}{t_0}\right)^{-m} . \quad (84d)$$

TABLE I. Summary of physical parameters used to constrain k-ϕ-L-a-V model coefficients.

α	Θ_{RT}	n	m	Φ^{-1}	$\delta/\mathcal{A}$	Θ_{KH}
0.06	0.80	1.11	1.33	0.035	0.08	0.80

Substituting Eqs. 84a through 84d back into Eqs. 80 through 83 leads to the following constraints after some algebra

$$\frac{C_D}{C_{L1}} = \frac{2n}{2-n}\,, \tag{85}$$

$$\frac{C_{p1}}{C_{L1}} = \frac{n}{n-2}\,, \tag{86}$$

$$\frac{C_{V2}}{C_{L1}} = \frac{2m}{2-n}\,. \tag{87}$$

D. Summary of constraints

Equations 31, 33, 48, 47, 51, 64, 69, 73, 79, and 85 through 87 represent 12 constraints on model coefficients C_{p3}, N_L, C_{V3}, C_A, C_B, C_{dev}, C_{V1}, C_{L3}, C_{p2}, and the ratios $\frac{C_D}{C_{L1}}$, $\frac{C_{p1}}{C_{L1}}$, and $\frac{C_{V2}}{C_{L1}}$ in terms of physical parameters α, Θ_{RT}, Θ_{KH}, Φ^{-1}, $\delta/\mathcal{A}$, n, and m. In addition, constraints have been determined on diffusion coefficients such that $N_p = N_L$, $N_k = 5N_L$, $N_p = 8N_L$, and $N_e = N_Y = N_a = N_k$. We have thus determined 18 constraints on the 20 model coefficients previously enumerated. To complete the model, the following constraint is applied to C_{L2} to ensure that the total velocity divergence contribution to the L equation is 1/3 [5, 16],

$$C_{L2} = \frac{1}{3} + \frac{2}{3}C_{L3}\,. \tag{88}$$

To resolve the remaining degree of freedom, a value should be chosen for C_{L1} or one of the dissipation coefficients C_D, C_{p1}, or C_{V2}. For simplicity, the present work takes $C_D = 1$, which completes the set of constraints on model coefficients for the k-ϕ-L-a-V model. Table I summarizes the values of physical parameters used, while Table II summarizes the full set of model coefficients through the similarity constraints. Note that by selecting a different value for C_D, one could derive a different set of model coefficients consistent with the physical parameters in Table I. The difference among such coefficient sets would be the value of the proportionality constant β, which effectively sets the scaling on most model coefficients.

IV. NUMERICAL RESULTS

The k-ϕ-L-a-V model is applied here to the simulation of several one-dimensional RT, RM, and KH test problems. The model is implemented in the *Ares* code, which is a second-order arbitrary Lagrangian/Eulerian (ALE) hydrodynamics code developed at Lawrence Livermore National Laboratory (LLNL) [12]. Results with the k-ϕ-L-a-V are compared with results obtained with the k-2L-a-V model [14–16, 22] to highlight differences that are realized due to the high-order spatial profiles of the k-ϕ-L-a-V model. While comparisons here are made against the k-2L-a-V model specifically, they should be considered representative comparisons for all "k-L-type" models which utilize the same assumptions of a linear mixing profile and quadratic TKE profile in their construction. In addition, model results are compared with data from large-eddy simulation (LES) or experiment where available.

A. Rayleigh-Taylor mixing layer

We first consider a one-dimensional hydrostatic RT mixing layer between two ideal, monatomic gases subject to constant acceleration at Atwood number $A_T = 0.05$. This problem is set up in a domain of size 1 cm with 1600 uniformly spaced computational zones. Turbulence length scales are initialized to zero everywhere except for the two zones bordering the interface at $y = 0$, where $L = \lambda_0 = 4.0 \times 10^{-6}$ cm. Turbulence kinetic energy is initialized to zero everywhere except the two interface zones, where k is initialized to 1.0 cm^2/s^2.

In Fig. 1a, the mixing layer width, the maximum turbulence kinetic energy K_0, and the maximum turbulence length scale L_0 are plotted for simulations using the k-2L-a-V and k-ϕ-L-a-V models. By plotting these quantities against $A_T g t^2$, they increase linearly, which implies quadratic growth of the form $\alpha A_T g t^2$. While the evolution of the mixing layer width h is nearly identical for both models, the magnitudes of K_0 and L_0 are uniformly lower for the k-ϕ-L-a-V model. Figure 1b illustrates that for both the k-2L-a-V and k-ϕ-L-a-V models, the realized growth parameter $\alpha = h/(A_T g t^2)$ asymptotes to the expected value 0.06, which was used to set the model coefficients. Figure 1c additionally plots the RT mixedness, as defined by Eq. 34 for both the k-2L-a-V and k-ϕ-L-a-V models. As expected, both models quickly achieve the self-similar value of $\Theta_{RT} = 0.8$. While the transient period is not very long for either model, the k-ϕ-L-a-V model demonstrates a somewhat shorter transient period. In Figs. 1b and 1c, the reference time $t_0 = \sqrt{\lambda_0/(A_T g)}$.

Figure 2 highlights the main difference between the k-2L-a-V and k-ϕ-L-a-V models as well as the chief advantage of the k-ϕ-L-a-V model. In Fig. 2, spatial profiles of heavy species mass fraction, normalized TKE, and scalar variance are plotted from 1D simulations using the two RANS models along with comparison profiles from LES

TABLE II. Model coefficients for the k-ϕ-L-a-V model.

C_{dev}	C_B	C_D	C_{L1}	C_{L2}	C_{L3}	C_{p1}	C_{p2}	C_{p3}	C_A	C_{V1}	C_{V2}	C_{V3}	$N_{Y,e,k,a}$	$N_{L,p}$	N_V
24.0	0.485	1.00	0.400	0.472	0.208	-0.500	3.44×10^{-4}	0.0576	0.893	30.5	1.20	0.985	0.0594	0.0119	0.0951

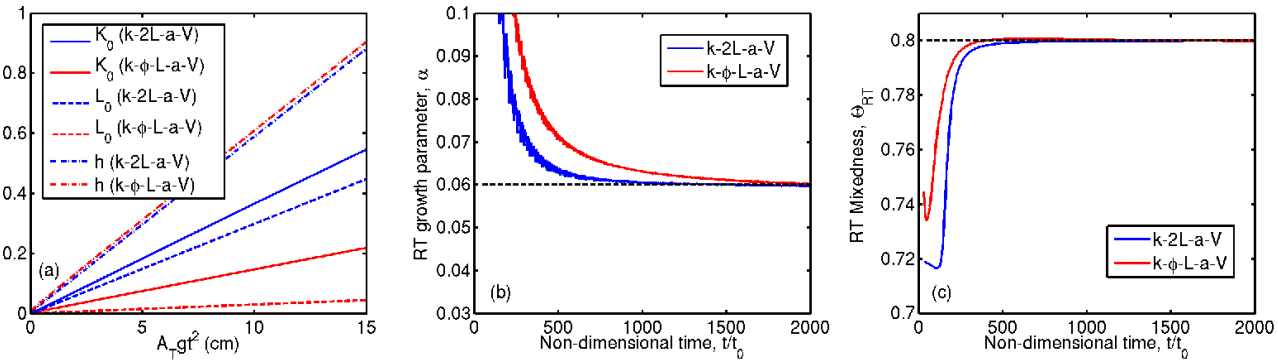

FIG. 1. Three measures of evolution of a 1D RT mixing layer. (a) Mixing layer half-width h, turbulence kinetic energy K_0, and turbulence length scale L_0 as a function of time for both the k-$2L$-a-V and k-ϕ-L-a-V models. Dimensions are in cm for h and L_0 but in $(\text{cm}/\mu\text{s})^2 \times 10^{-9}$ for K_0. (b) The RT growth parameter, $\alpha = h/(A_T g t^2)$ is plotted as a function of non-dimensional time for both k-$2L$-a-V and k-ϕ-L-a-V models. (c) Steady-state mixedness with both the k-$2L$-a-V and k-ϕ-L-a-V models.

by Morgan *et al.* [27]. As these plots show, the high-order spatial profiles realized by the k-ϕ-L-a-V model match much more closely with the LES results than the k-$2L$-a-V results. While the peak magnitude in scalar variance (Fig. 2c) with k-ϕ-L-a-V appears slightly over-predicted with respect to LES, it is interesting to recall that the steady-state mixedness of both RANS solutions is exactly 0.8. Given the close agreement between LES and k-ϕ-L-a-V in the spatial profile of $\widetilde{Y}_H$, one must conclude that the mixedness of the comparison LES is slightly greater than 0.8.

Figures 3 through 5 demonstrate the impact of increasing Atwood number on spatial profiles of heavy species mass fraction, normalized TKE, and scalar variance. In each of these figures, results with the k-$2L$-a-V model are plotted on the left, and results with the k-ϕ-L-a-V model are plotted on the right. As the k-ϕ-L-a-V model is pushed towards higher Atwood number, the spatial profiles stay smooth due to the high-order nature of the self-similarity solution. With the k-$2L$-a-V model, the magnitude of discontinuity in the first-derivative of spatial profiles becomes exaggerated around $\chi = -1$, which could impact problem stability at higher Atwood number. In addition, the k-$2L$-a-V profiles demonstrate some amount of drift away from $\chi = 0$ (previously observed with the k-L-a model as well [10]), which is not present in the k-ϕ-L-a-V model results.

B. Richtmyer-Meshkov mixing layer

We next consider simulation of the Mach 1.5 air/SF_6 shock tube experiment ($A_T \approx 0.67$) by Vetter and Sturtevant [28]. The shockwave is driven from air into SF_6, reflected from the end wall, and eventually re-shocks the fluid interface. In this particular experiment, a rarefaction wave additionally interacts with the mixing layer shortly after the second shock.

Simulation results are found to be well-converged with 2560 zones in the 60.0 cm SF_6 test section, 3840 zones of shocked air (157 cm), and 80 zones of ambient air (6.0 cm). An initially diffuse interface of width $h_0 = 0.11$ cm is assumed, and the initial conditions are

$$\begin{aligned} Y_{SF_6}(y,0) &= \frac{1}{2}\left[1+\tanh\left(\frac{y}{h_0}\right)\right], \\ L(y,0) &= 4\,\lambda_0\,Y_{SF_6}(y)\,[1-Y_{SF_6}(y)] \\ k(y,0) &= 4\,k_0\,Y_{SF_6}(y)\,[1-Y_{SF_6}(y)]\,. \end{aligned} \tag{89}$$

The initial length scales and turbulence kinetic energy are initialized with a smooth profile, where $k_0 = 1.0\times10^{-6}$ $\text{cm}^2/\mu\text{s}^2$, and λ_0 is chosen to give nearly the same behavior on first shock for both models. For the k-$2L$-a-V model, $\lambda_0 = 0.11$ cm, and for the k-ϕ-L-a-V model, $\lambda_0 = 0.02$ cm.

Mixing layer width as a function of time is plotted for both RANS models in Fig. 6 and compared against experimental data from Vetter and Sturtevant [28]. By design, initial conditions have been selected for both models to give nearly identical behavior on first shock and to pass roughly through the first-shock experimental data points. When compared in this way, the k-ϕ-L-a-V model is observed to predict somewhat less growth immediately after the second shock has passed. The most likely reason for this difference seems to be the smoother profiles achieved

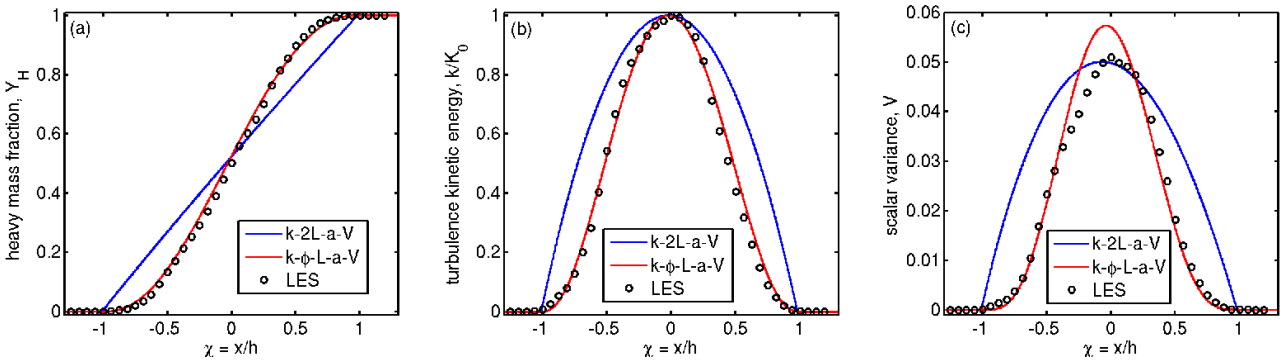

FIG. 2. Comparison of RT spatial profiles between the k-2L-a-V model, the k-ϕ-L-a-V model, and LES by Morgan *et al.* [27]: (a) average mass fraction of the heavy species, $\widetilde{Y}_H$, (b) normalized turbulence kinetic energy k/K_0, and (c) scalar variance $V = \widetilde{Y_H'' Y_H''}$ are all plotted versus the spatial similarity variable $\chi = x/h$.

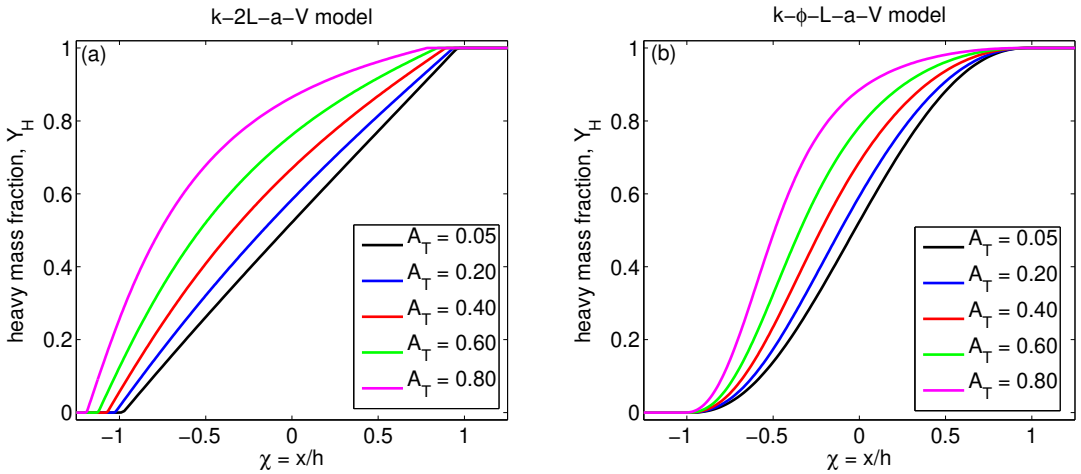

FIG. 3. Comparison of spatial profiles of heavy species mass fraction Y_H in an RT mixing layer with increasing Atwood number: (a) with the k-2L-a-V model and (b) with the k-ϕ-L-a-V model.

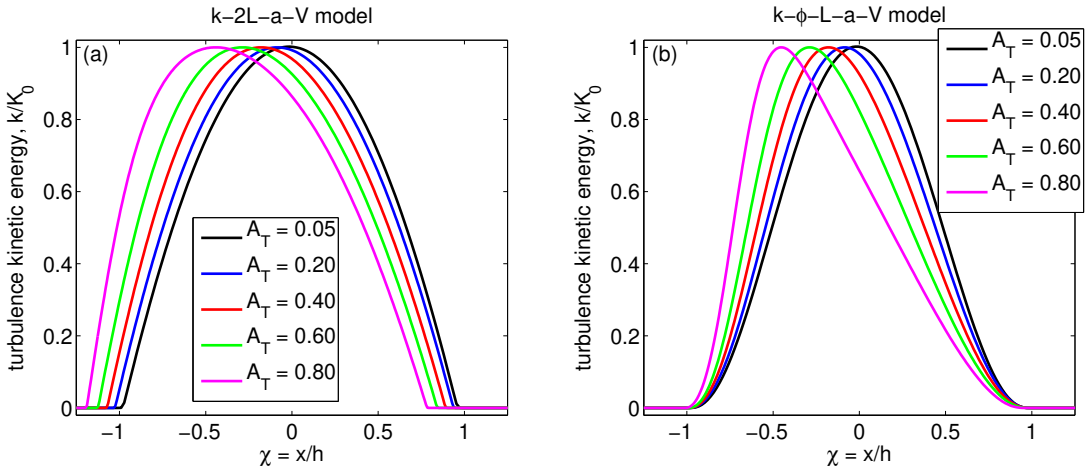

FIG. 4. Comparison of spatial profiles of normalized TKE, k/K_0, in an RT mixing layer with increasing Atwood number: (a) with the k-2L-a-V model and (b) with the k-ϕ-L-a-V model.

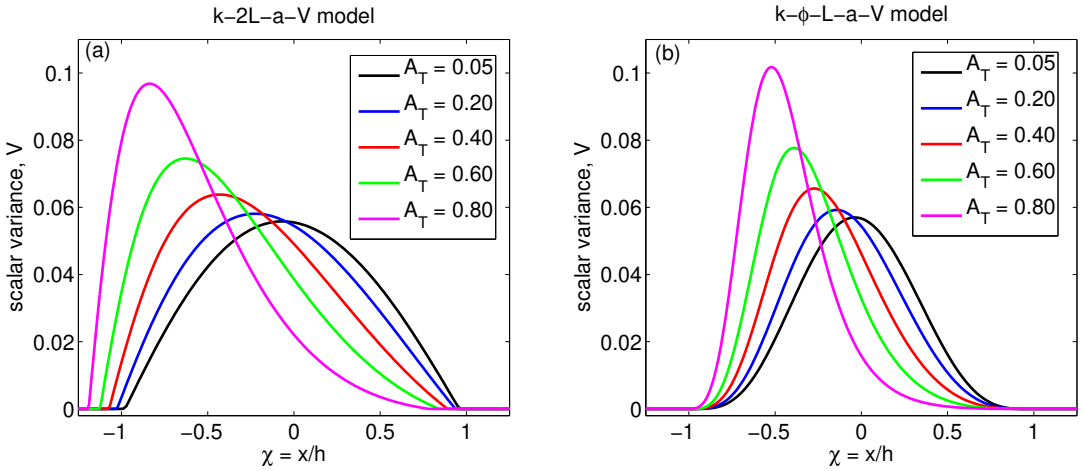

FIG. 5. Comparison of spatial profiles of scalar variance V, in an RT mixing layer with increasing Atwood number: (a) with the k-2L-a-V model and (b) with the k-ϕ-L-a-V model.

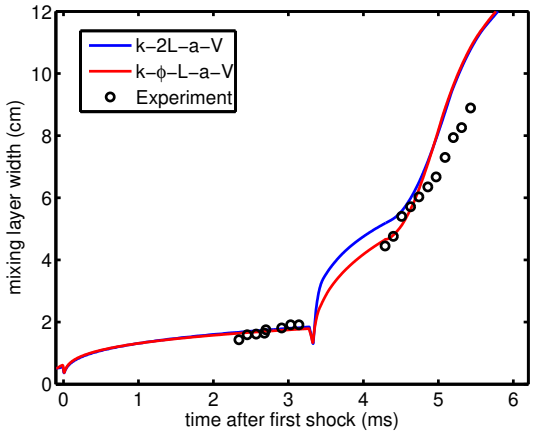

FIG. 6. Mixing width as a function of time for the Vetter and Sturtevant shock tube experiment [28]. Symbols indicate experimental data, while solid lines indicate simulation results with the k-2L-a-V and k-ϕ-L-a-V models.

by the k-ϕ-L-a-V model, highlighted previously in Figs. 3 through 5, which should lead to reduced-magnitude gradients that appear in buoyancy production mechanisms during shock passage. As a result, for this particular selection of initial conditions, the k-ϕ-L-a-V mixing layer width passes more-or-less through the cloud of second-shock data points. Of course it is worth pointing out that by reducing the choice of λ_0 for the k-2L-a-V model, it is possible to achieve a nearly equivalent result for the second-shock data points with a lower crossing point through the first-shock data.

C. Kelvin-Helmholtz mixing layer

Next, we consider KH mixing layer simulations run with 960 uniformly-spaced computational zones on a domain extending from $y = -48.0$ cm to $y = 48.0$ cm. Turbulence length scales are initialized to zero everywhere except for the two zones bordering the interface at $y = 0$, where $L = 0.44$ cm. Turbulence kinetic energy is additionally initialized to zero everywhere except for the two interface zones, where k is initialized to $0.01\,(\Delta U)^2$. The initial velocity profile is chosen to match the Bell and Mehta experiment [29] such that $\widetilde{u}_x = U_1 = 900$ cm/s for $y < 0$ and $\widetilde{u}_x = U_2 = 1500$ cm/s for $y \geq 0$, corresponding to $\mathcal{A} = 0.25$.

Figures 7 and 8 compare the basic measures of self-similar behavior expected for a KH mixing layer between the k-2L-a-V and k-ϕ-L-a-V models. In Fig. 7, the mixing layer width as a function of time is plotted along with the non-dimensional growth parameter $\delta/\mathcal{A}$. From Fig. 7b, it is clear that both models approach the expected growth parameter of $\delta/\mathcal{A} = 0.08$ and therefore result in the same KH growth rate. However, the k-ϕ-L-a-V model is observed to have a shorter transient period and reach the self-similar state quite a bit sooner than the k-2L-a-V model. Similar behavior is observed in Figs. 8a and 8b as well. These figures plot, respectively, the KH mixedness and the turbulence intensity $k/\left(\Delta U\right)^2$ as a function of time. Both models are observed to reach the same expected self-similar values, 0.8 for the KH mixedness and 0.035 for the turbulence intensity. As with the growth parameter, however, the k-ϕ-L-a-V model demonstrates a shorter transient period and reaches the steady-state much sooner. Recall from Fig. 1a that in the 1D RT simulations, at effectively the same mixing layer width, the k-ϕ-L-a-V model predicted a lower magnitude for both L_0 and K_0 compared to the k-2L-a-V model. Similar behavior was observed in the RM results illustrated in Fig. 6, where the initial turbulence

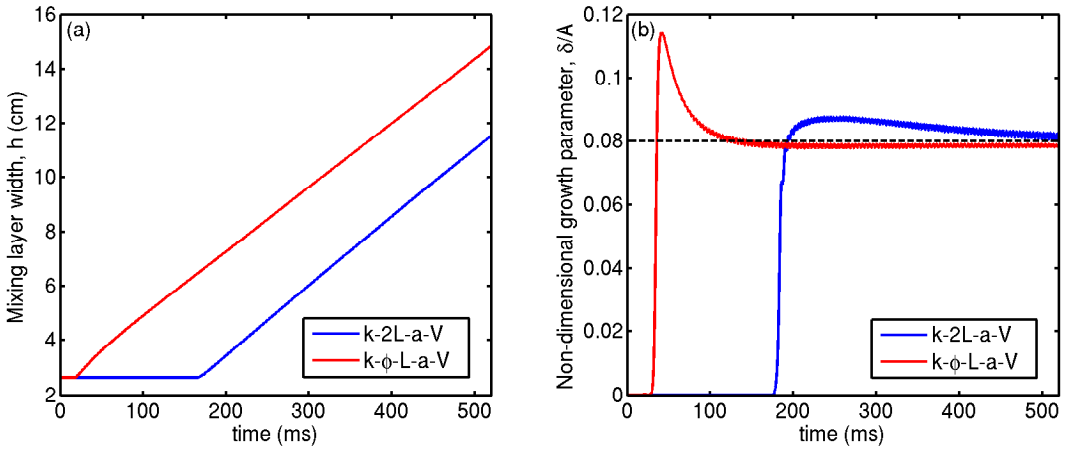

FIG. 7. Mixing layer growth in a 1D KH mixing layer. (a) Mixing layer half-width h as a function of time for both the k-2L-a-V and k-ϕ-L-a-V models. (b) KH growth parameter $\delta/\mathcal{A}$ as a function of time for both k-2L-a-V and k-ϕ-L-a-V models.

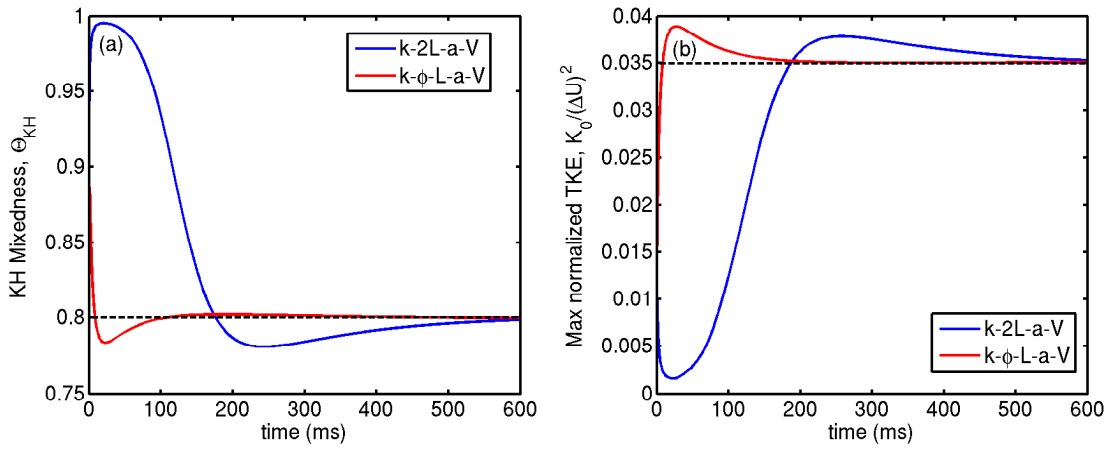

FIG. 8. Two measures of evolution in a psuedo-1D KH mixing layer with both the k-2L-a-V and k-ϕ-L-a-V models: (a) steady-state mixedness and (b) steady-state turbulence intensity, $k/\left(\Delta U\right)^2$.

length scale needed by the k-ϕ-L-a-V model was about a factor of five less than that of the k-2L-a-V model to achieve the same first-shock growth. This behavior indicates that the proportionality constant β is greater for the k-ϕ-L-a-V model than the k-2L-a-V model. Thus, in the present KH simulation results in which both models are initialized with the same value of L, the k-ϕ-L-a-V model grows the mixing layer width more rapidly initially until it becomes resolved and begins to grow self-similarly. As a result, the transient period is observed to be shorter.

Spatial profiles of average streamwise velocity $\widetilde{u}_x$ and TKE are plotted in Fig. 9 with comparison results from LES by Morgan [22]. As before with the RT profiles, the high-order spatial profiles realized with the k-ϕ-L-a-V model demonstrate much closer agreement with the LES than the k-2L-a-V results. One interesting aspect of the comparisons in Fig. 9b is that the TKE profile from LES appears to extend beyond the bounds of the spatial similarity variable $\chi \in [-1, 1]$, a characteristic which can also be observed in experimental data by Bell and Mehta [29]. This behavior is in contrast to the RT case (Fig. 2b) and could suggest that KH intermittency effects are still not fully accounted for in the present similarity analysis. However, the difference between RANS and LES TKE profiles is nonetheless much improved with the k-ϕ-L-a-V model.

D. Combined Rayleigh-Taylor–Kelvin-Helmholtz mixing

In order to consider model behavior during transition between shear-dominated mixing and buoyancy-dominated mixing, the k-ϕ-L-a-V model is now applied to the simulation of combined RT-KH instability. In this case, the relative strength of buoyancy to shear effects is given by the Richardson number,

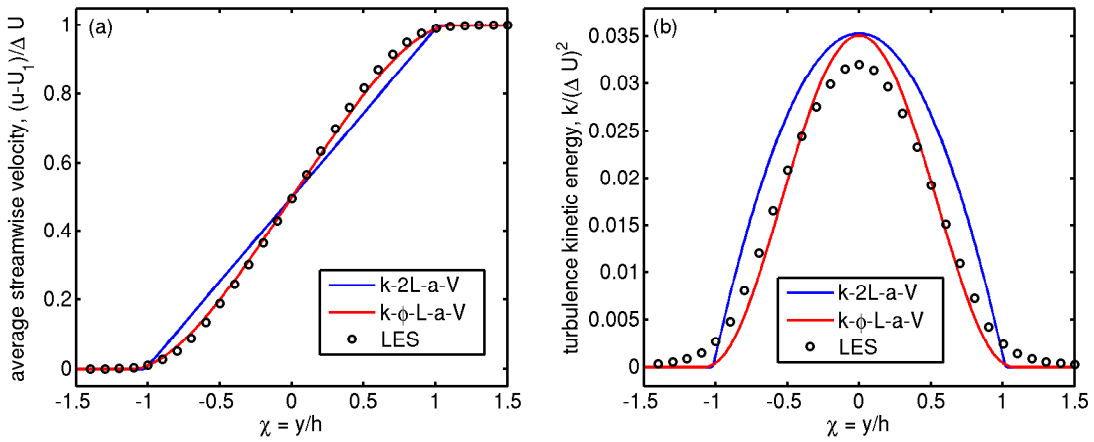

FIG. 9. Comparison of RT spatial profiles between the k-2L-a-V model, the k-ϕ-L-a-V model, and LES by Morgan [22]: (a) average streamwise velocity, $\widetilde{u}_x$, and (b) normalized turbulence kinetic energy $k/\left(\Delta U\right)^2$ are plotted versus the spatial similarity variable $\chi = y/h$.

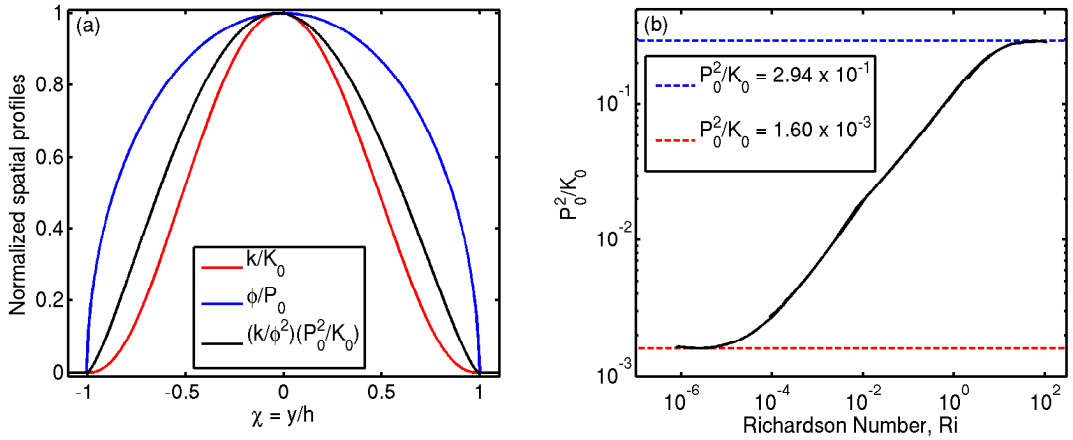

FIG. 10. Two representations of the relationship between the turbulence velocities ϕ and $\sqrt{k}$ in a combind RT-KH mixing layer: (a) normalized spatial profiles and (b) the magnitude of $\frac{P_0^2}{K_0}$ as a function of Richardson number.

$$\mathrm{Ri} = -\frac{g\partial\overline{\rho}/\partial y}{\left(\partial\tilde{u}/\partial y\right)^2} \approx -\frac{2gA_Th}{\left(\Delta U\right)^2}\,. \tag{90}$$

A quasi-1D mixing layer is simulated at $A_T = 0.05$ and $\mathcal{A} = 0.50$ for varying intensity of gravitational acceleration. Figure 10 provides two representations of the relationship between the two turbulence velocities, ϕ and $\sqrt{k}$, and how this relationship changes as a function of Richardson number. In Fig. 10a, normalized spatial profiles of k and ϕ are plotted along with the normalized ratio $\frac{k}{\phi^2}$. As expected, k conforms to an $f^{5/2}$ profile, and ϕ conforms to an $f^{1/2}$ profile; thus, the ratio k/ϕ^2 assumes a profile of the form $f^{3/2}$. The magnitude of the normalization factor $\frac{P_0^2}{K_0}$, however, is given by Eq. 46 in the limit of RT mixing and by Eqs. 72 and 76 in the limit of KH mixing. Substitution of the values in Tables I and II into these equations gives expected limits of $\frac{P_0^2}{K_0} \approx 1.60\times10^{-3}$ for KH flow and and $\frac{P_0^2}{K_0} \approx 2.94\times10^{-1}$ for RT flow.

Figure 10b plots the magnitude of the normalization factor $\frac{P_0^2}{K_0}$ as a function of Richardson number. Note that the black curve in Fig. 10b is generated as a composite from several different simulations with varying intensity of gravitational acceleration that overlap across Richardson numbers. From this figure, we see that $\frac{P_0^2}{K_0}$ varies smoothly between the expected limits as Richardson number increases from the shear-dominated regime to the buoyancy-dominated regime. Similar behavior was observed for the ratio of length scales in simulations of combined RT-KH mixing with the k-2L-a model [14]. Specifically, with the k-2L-a model, the ratio of the destruction length scale L_d to the transport length scale L_t was found to vary between two constant limits as the

Richardson number is increased from shear-dominated to buoyancy-dominated flow. We observe that the two turbulence velocities in the present k-ϕ-L-a-V model play a similar role to the two turbulence length scales in the k-$2L$-a model in allowing the smooth transition between shear-dominated and buoyancy-dominated flow.

More generally, the magnitude of the ratio $\frac{\phi^2}{k}$ is interesting as a potential diagnostic because of this behavior. Since $\frac{\phi^2}{k}$ is expected to vary between two known self-similar values, the magnitude of this ratio in more complicated simulations might provide some indication about whether local mixing behavior is dominated by shear or buoyancy effects.

V. SUMMARY AND CONCLUSIONS

The present work has introduced a new RANS model for variable density turbulent mixing, termed the k-ϕ-L-a-V model. This new model differs from other similar models in that it has been designed to relax the assumption of a linear mixing profile. In contrast to models which have attempted to achieve similar behavior through *ad hoc* adjustment of diffusion coefficients, the k-ϕ-L-a-V model achieves high-order spatial profiles that are self-consistent with similarity analysis. This allows one to determine model coefficients that will exactly reproduce desired growth rates while maintaining high-order spatial profiles. Although the present model utilizes a transport equation for scalar mass fraction variance V, it is worth noting that the present approach could alternatively be applied to construct a similar model that might instead solve for density variance, temperature variance, or the density-specific-volume covariance, b.

In Section III, a full description of the self-similarity analysis for the k-ϕ-L-a-V model was presented, and a complete set of constraints were determined for model coefficients. Using these self-similarity constraints, a set of model coefficients was then determined based on seven physical growth and decay parameters from RT mixing, KH mixing, and homogeneous isotropic turbulence. The k-ϕ-L-a-V model was then applied in simulations of RT, RM, and KH mixing layers and compared with results from the k-$2L$-a-V model. Through these comparisons, it was shown that the expected growth parameters were recovered exactly and that, in contrast to the k-$2L$-a-V results, the high-order spatial profiles achieved by the k-ϕ-L-a-V model agreed more closely with data from high-fidelity LES. In addition, it was found that transient behavior prior to achieving steady-state behavior tended to be shorter with the k-ϕ-L-a-V, and smooth spatial profiles persisted at higher Atwood numbers which could potentially contribute to improved numerical stability and reduced spurious growth.

While many practical problems of variable density mixing may only be sensitive to low-order effects such as mixing layer growth rates, work by Mackay and Pino [30] has suggested that a linear mixing profile in applications of inertial confinement fusion could contribute to inaccuracy in predicting higher-order observables such as the reaction-weighted ion temperature. In this regard, the k-ϕ-L-a-V model might be expected to behave better than a model with linear spatial profiles like k-$2L$-a-V. Of course, this remains to be shown and should be explored in future work.

ACKNOWLEDGMENTS

This work was performed under the auspices of the U.S. Department of Energy by Lawrence Livermore National Laboratory under Contract No. DE-AC52-07NA27344.

Appendix A: Model extension for multicomponent mixing

It is possible to formulate the k-ϕ-L-a-V model in such a way that it is not restricted to only two-fluid mixing. Broadly speaking, the manner in which this extension is approached is to replace the two-fluid closure for b with the multifluid closure utilized by the k-L-a model [10]. In addition, the shear production term involving gradient of mass fraction in Eq. 12 is replaced by the gradient of density, and production terms involving V are summed over all components. Eqs. A1 through A3 summarize the multicomponent extension of the k-ϕ-L-a-V model.

$$\begin{aligned}\overline{\rho}\frac{D\phi}{Dt} =& C_{p1}\overline{\rho}\frac{\phi^2}{L} + C_{p2}\frac{1}{\phi\sum_\alpha V_\alpha^{3/8}}\overline{\rho}\tau_{ij}\frac{\partial\widetilde{u}_i}{\partial x_j} \\ &+ C_{p3}\frac{a_i}{\phi\sum_\alpha V_\alpha^{3/8}}\frac{\partial\overline{p}}{\partial x_i} + \frac{\partial}{\partial x_i}\left(\frac{\mu_t}{N_p}\frac{\partial\phi}{\partial x_i}\right) , \end{aligned} \tag{A1}$$

$$\begin{aligned}\overline{\rho}\frac{Da_j}{Dt} =& C_B\frac{b}{\sum_\alpha V_\alpha^{3/8}}\frac{\partial\overline{p}}{\partial x_j} - C_A\overline{\rho}\frac{\phi}{L}a_j \\ &+ \frac{\tau_{ij}}{\sum_\alpha V_\alpha^{3/8}}\frac{\partial\overline{\rho}}{\partial x_i} + \frac{\partial}{\partial x_i}\left(\frac{\mu_t}{N_a}\frac{\partial a_j}{\partial x_i}\right) , \end{aligned} \tag{A2}$$

$$b = \overline{\rho}\frac{\sum_\alpha \frac{v_\alpha}{\rho_\alpha + c\overline{\rho}}}{\sum_\alpha \frac{v_\alpha\rho_\alpha}{\rho_\alpha + c\overline{\rho}}} - 1 . \tag{A3}$$

In Eq. A3, c is a correction factor term that can be used to avoid the closure diverging at high Atwood number. For low and moderate Atwood number $c = 0$. Note that since the similarity analysis in section III utilizes an ansatz on the form of the mass-fraction profile rather than the volume-fraction profile, the effect of replacing mass fraction gradients with the density gradients in Eq. A2 is that the self-similarity results determined in section III will only approximately hold for the multicomponent extension except in the limit of low Atwood number where $v_\alpha \approx Y_\alpha$.

[1] D. Besnard, F. H. Harlow, and R. Rauenzahn, *Conservation and Transport Properties of Turbulence with Large Density Variations*, Tech. Rep. LA-10911-MS (Los Alamos National Laboratory, 1987).

[2] S. Gauthier and M. Bonnet, "A k-ε model for turbulent mixing in shock-tube flows induced by Rayleigh-Taylor instability," Phys. Fluids A **2**, 1685–1694 (1990).

[3] D. C. Besnard, F. H. Harlow, R. M. Rauenzahn, and C. Zemach, *Turbulence transport equations for variable-density turbulence and their relationship to two-field models*, Tech. Rep. LAUR-12303 (Los Alamos National Laboratory, 1992).

[4] O. Grégoire, D. Souffland, and S. Gauthier, "A second-order turbulence model for gaseous mixtures induced by Richtmyer-Meshkov instability," J. Turbul. **6**, 1–20 (2005).

[5] G. Dimonte and R. Tipton, "K-L turublence model for the self-similar growth of the Rayleigh-Taylor and Richtmyer-Meshkov instabilities," Phys. Fluids **18**, 085101 (2006).

[6] A. Banerjee, R. A. Gore, and M. J. Andrews, "Development and validation of a turbulent-mix model for variable-density and compressible flows," Phys. Rev. E **82**, 046309 (2010).

[7] J. D. Schwarzkopf, D. Livescu, R. A. Gore, R. M. Rauenzahn, and J. R. Ristorcelli, "Application of a second-moment closure model to mixing processes involving multicomponent miscible fluids," J. Turbul. **12**, 1–35 (2011).

[8] B. M. Haines, F. F. Grinstein, and J. D. Schwarzkopf, "Reynolds-averaged Navier-Stokes initialization and benchmarking in shock-driven turublent mixing," J. Turbul. **14**, 46–70 (2013).

[9] I. W. Kokkinakis, D. Drikakis, D. L. Youngs, and R. J. R. Williams, "Two-equation and multi-fluid turbulence models for Rayleigh-Taylor mixing," Int. J. Heat Fluid Flow **56**, 233–250 (2015).

[10] B. E. Morgan and M. E. Wickett, "Three-equation model for the self-similar growth of Rayleigh-Taylor and Richtmyer-Meshkov instabilities," Phys. Rev. E **91**, 043002 (2015).

[11] J. D. Schwarzkopf, D. Livescu, J. R. Baltzer, R. A. Gore, and J. R. Ristorcelli, "A two-length scale turbulence model for single-phase multi-fluid mixing," Flow Turbul. Combust. **96**, 1–43 (2016).

[12] B. E. Morgan J. A. Greenough, "Large-eddy and unsteady RANS simulations of a shock-accelerated heavy gas cylinder," Shock Waves **26**, 355–383 (2016).

[13] O. Schilling and N. J. Mueschke, "Turbulent transport and mixing in transitional Rayleigh-Taylor unstable flow: *A priori* assessment of gradient-diffusion and similarity modeling," Phys. Rev. E **96**, 063111 (2017).

[14] B. E. Morgan, O. Schilling, and T. A. Hartland, "Two-length-scale turbulence model for self-similar buoyancy-, shock-, and shear-driven mixing," Phys. Rev. E **97**, 013104 (2018).

[15] B. E. Morgan, B. J. Olson, W. J. Black, and J. A. McFarland, "Large-eddy simulation and Reynolds-averaged Navier-Stokes modeling of a reacting Rayleigh-Taylor mixing layer in a spherical geometry," Phys. Rev. E **98**, 033111 (2018).

[16] A. Campos and B. E. Morgan, "Direct numerical simulation and Reynolds-averaged Navier-Stokes modeling of the sudden viscous dissipation for multicomponent turbulence," Phys. Rev. E **99**, 063103 (2019).

[17] I. W. Kokkinakis, D. Drikakis, and D. L. Youngs, "Modeling of Rayleigh-Taylor mixing using single-fluid models," Phys. Rev. E **99**, 013104 (2019).

[18] I. W. Kokkinakis, D. Drikakis, and D. L. Youngs, "Two-equation and multi-fluid turbulence models for Richtmyer-Meshkov mixing," Phys. Fluids **32**, 074102 (2020).

[19] M. Xiao, Y. Zhang, and B. Tian, "Unified prediction of reshocked Richtmyer-Meshkov mixing with K-L model," Phys. Fluids **32**, 032107 (2020).

[20] M. Xiao, Y. Zhang, and B. Tian, "Modeling of turbulent mixing with an improved K-L model," Phys. Fluids **32**, 092104 (2020).

[21] Y. Zhang, Z. He, H. Xie, M.-J. Xiao, and B. Tian, "Methodology for determining coefficients of turbulent mixing model," J. Fluid Mech. **905**, A26 (2020).

[22] B. E. Morgan, "Scalar mixing in a Kelvin-Helmholtz shear layer and implications for Reynolds-averaged Navier-Stokes modeling of mixing layers," Phys. Rev. E **103**, 053108 (2021).

[23] J. C. Rotta, "Statistiche theorie nichthomogener turbulenz," Z. Phys. **129**, 547–572 (1951).

[24] G. L. Mellor and H. J. Herring, "Survey of the mean turbulent field closure models," AIAA Journal **11**, 590–599 (1973).

[25] L. H. Kantha, "The length scale equation in turbulence models," Nonlinear Process. Geophys. **11**, 83–97 (2004).

[26] U. Goldberg, P. Batten, and S. Palaniswamy, "The q-l turbulence closure for wall-bounded and free shear flows," in *42nd AIAA Aerospace Sciences Meeting and Exhibit*, AIAA 2004-269 (2004).

[27] B. E. Morgan, B. J. Olson, J. E. White, and J. A. McFarland, "Self-similarity of a Rayleigh-Taylor mixing layer at low Atwood number with a multimode initial perturbation," J. Turbul. **18**, 973–999 (2017).

[28] M. Vetter and B. Sturtevant, "Experiments on the Richtmyer-Meshkov instability of an air/SF_6 interface," Shock Waves **4**, 247–252 (1995).

[29] J. H. Bell and R. D. Mehta, "Development of a two-stream mixing layer from tripped and untripped boundary layers," AIAA Journal **28**, 2034–2042 (1990).

[30] K. K. Mackay and J. E. Pino, "Modeling gas-shell mixing in ICF with separated reactants," Phys. Plasmas **27**, 092704 (2020).